Ultrafast pulse interactions with two-level atoms

Richard W. Ziolkowski
Department of Electrical and Computer Engineering, University of Arizona, Tucson, Arizona 85721

John M. Arnold
Department of Electronics and Electrical Engineering, University of Glasgow, Glasgow, Scotland, United Kingdom

Daniel M. Gogny
Commissariat a L'Energie Atomique, Centre d'Études Scientifiques et Techniques d'Aquitaine, Boîte Postale 2, Le Barp 33114, France
(Received 9 January 1995)

An iterative predictor-corrector finite-difference time-domain method is used to solve the semiclassical Maxwell-Bloch system numerically without invoking any of the standard approximations such as the rotating-wave approximation. This approach permits a more exact study of self-induced transparency effects in a two-level atom. In addition to recovering the standard results, for instance, for π, 2π, and 4π pulses, several features in the results appear at the zeros of the driving pulse, where its time derivatives are maximum. Several ultrafast-pulse examples demonstrate that time-derivative-driven nonlinearities have a significant impact on the time evolution of a two-level atom system. Moreover, typical small-signal gain results are also obtained with our Maxwell-Bloch simulator. We illustrate that these time-derivative effects can be used to design an ultrafast, single-cycle pump pulse that completely inverts the two-level atom population. A pump-probe signal set is then used to illustrate gain in the probe signal.

PACS number(s): 42.50.Md, 42.50.Rh, 42.50.Hz, 32.80.−t

I. INTRODUCTION

Nonlinear optical (NLO) devices are currently being explored for their applications in various systems associated with communications, remote sensing, optical computing, etc. However, as the size of the optical devices is pushed to the size of an optical wavelength and less, the need for more exact materials and response models is tantamount to the successful design and fabrication of those devices. Most current simulation models are based on known macroscopic, phenomenological models that avoid issues dealing with specific microscopic behavior of the materials in such NLO devices. Inaccuracies in the simulation results are then exacerbated as the device sizes shrink to subwavelength sizes and the response times of the excitation signals surpass the response times of the material. There are laser sources currently under development with submicrometer wavelengths that are pushing the boundaries of the subfemtosecond regime. Phenomenological nonresonant models lose their ability to describe the physics in this parameter regime; hence, they lose their accuracy there. Quantum-mechanical effects begin to manifest themselves; the simulation models must incorporate this behavior to be relevant.

The problem of accurate numerical modeling of NLO devices has been subject to increasing interest in recent years. Since the most interesting nonlinear phenomena are transient and superposition is not available, it is natural to try to carry out this modeling directly in the time domain. For this reason the finite-difference time-domain (FDTD) method is receiving intensive study (see, for example, [1–11]). In contrast to the case for frequency-domain linear analysis, a single value of permittivity ϵ is completely inadequate to describe nonlinear time-dependent phenomena, and it is essential to model the interaction of the electromagnetic field with the material medium. To understand these small-distance-scale and short-time-scale interactions, particularly in the resonance regime of the materials and the associated device structures, a first-principles approach is desirable. This in turn requires quantum-mechanical descriptions of the electronic states available in the medium. Physical models incorporate all propagation effects such as dispersion and nonlinearity, with the proper physical linkages between them.

In this paper we utilize the Maxwell-Bloch system which couples the Maxwell equations with a two-level atom model for the polarization. The two-level atom has been studied extensively in the past (some representative references include [12–21]) and has been used for pulse dynamical effects in recent guide-star applications [22–24]. The present effort is different in that it combines a realistic material model that is quantum-mechanically based with a full-wave vector Maxwell's equations solver. The FDTD implementation of the Maxwell-Bloch modeling system is relatively straightforward, but it also yields some interesting physical consequences to which our paper is addressed. Both Fleck [15] and Eilbeck and Bullough [17] have also solved the Maxwell-Bloch system numerically, but in both cases the method of characteristics was used. The latter involves the simultaneous treatment of both forward- and backward-propagating waves rather than solving the original Maxwell-Bloch system directly. Fleck [15] further introduced a truncated Fourier series expansion for the various terms in this system, made a rotating-wave approximation, and then solved the resulting system for the Fourier coefficients with a finite-difference approach in the time domain. On the other hand, Eilbeck and Bullough [17] integrated the equivalent characteristic form of the Maxwell-Bloch system directly in the time domain with a finite-difference approach. In the same manner the FDTD approach solves the Maxwell-Bloch

system directly in the time domain, but it invokes neither the rotating-wave approximation nor the decomposition into characteristic waves.

Several examples will be presented which will illustrate the advantages of the self-consistent microscopic materials and macroscopic electromagnetics response model represented by the coupled Maxwell-Bloch system. These will include configurations that produce π, 2π, and 4π self-induced transparency (SIT) effects. These problems depend intimately upon the quantum-mechanical effects associated with the two-level atomic system model; the SIT results are not realizable with purely phenomenological macroscopic material models. The model includes nonlinearity, dispersion, dissipation (or amplification), saturation, and resonance effects. The one-dimensional versions of these SIT problems have known rotating-wave and other approximate solutions which are used to guide and validate the present numerical analyses. New features present in the full-wave solutions that are absent in these standard approximate models are explained from first principles. It will be shown that the time derivatives of the electric fields of the SIT pulses play an essential role in the nonlinear evolution of the system. These time-derivative features are then emphasized through the use of ultrafast- (single-cycle-) pulse excitations. We use these time-derivative characteristics of the two-level atom model to design an ultrafast, single-cycle pulse that completely inverts the two-level atom population. Additional ultrafast pulse examples will demonstrate that the time-derivative-driven nonlinearities have a significant impact on the nonlinear evolution of the two-level atom medium.

We also consider small-signal gain conditions which are obtainable from the two-level atom model. Known [25] results are recovered. We then simulate a pump-probe configuration. We design a pulse set that uses an ultrafast, single-cycle pulse to pump the medium into an inverted state; a trailing probe pulse then experiences the expected small-signal gain.

II. THE MAXWELL-BLOCH SYSTEM

The starting point for the implementation of linear or nonlinear electromagnetics is the Maxwell equations

$$\partial_t \vec{H} = -\frac{1}{\mu_0}\vec{\nabla}\times\vec{E},$$

$$\partial_t \vec{E} = \frac{1}{\epsilon_0}\vec{\nabla}\times\vec{H} - \frac{1}{\epsilon_0}\partial_t \vec{P}. \tag{1}$$

The polarization $\vec{P}$ is given by

$$\vec{P}(\vec{r},t) = -N_{\text{atom}} e \vec{q}(\vec{r},t), \tag{2}$$

where N_{atom} is the density of polarizable atoms and $-e$ is the electronic charge. For the classical description $\vec{q}(\vec{r},t)$ is the displacement from equilibrium of an electron in the atom at the equilibrium position $\vec{r}$. In quantum-mechanical descriptions of the atom, the displacement $\vec{q}(\vec{r},t)$ is expressed as the expectation of a time-independent operator $\vec{Q}$ with respect to the quantum state $\Psi(\vec{r},t)$. In particular, let the state vector $\Psi(\vec{r},t)$ exist in a Hilbert space $\mathscr{H}$ with inner product $\langle\ ,\ \rangle$. It evolves in time according to the time-dependent Schrödinger equation

$$i\hbar\partial_t \Psi = H\Psi, \tag{3a}$$

where the Hamiltonian operator $H = H_0 + e\vec{E}\cdot\vec{Q}$ is composed of an unperturbed part H_0 representing the behavior of the atom when no field is present, and a dipole interaction term $H_{\text{int}} = e\vec{E}\cdot\vec{Q}$. The expectation value of the position operator is then

$$\vec{q} = \langle\vec{Q}\rangle = \langle\Psi, \vec{Q}\Psi\rangle. \tag{3b}$$

The unperturbed Hamiltonian H_0 can usually be assumed to be a diagonal operator. The determination of $\vec{q}(\vec{r},t)$ requires determination of $\Psi(\vec{r},t)$.

It is often more convenient to use the density-of-states operator ρ in place of the state vector Ψ. Then the Schrödinger equation is replaced by the Liouville equation

$$i\hbar\partial_t \rho = [H,\rho], \tag{4a}$$

in which the commutator operation $[A,B] = AB - BA$. The expectation value of the displacement operator now becomes

$$\vec{q} = \langle\vec{Q}\rangle = \text{Tr}\{\rho\vec{Q}\}, \tag{4b}$$

where Tr represents the trace operation (sum of diagonal elements).

In the FDTD method the spatial derivatives in (1) are replaced by discretized operators acting on samples defined on a spatial grid. The resulting system of ordinary differential equations is then integrated stepwise in time. This requires the evaluation of the polarization $\vec{P}$ at each time step, and hence the solution of the additional system of ordinary differential equations (3) or (4). An important consideration in integrating large systems of differential equations over a very large number of steps is that the solutions should remain stable.

The Schrödinger equation (3) and the Liouville equation (4) can be integrated by identical methods provided that the Hamiltonian H is expanded in the adjoint representation of the Lie algebra SU(n), where n is the number of discrete energy levels of the quantum system. For the Liouville equation this leads to the system

$$\partial_t \hat{\rho} = \hbar^{-1}\hat{H}\hat{\rho}, \tag{5}$$

where $\hat{\rho}$ is the (n^2-1)-dimensional vector representing the operator $-i\rho$ and $\hat{H}$ is the $n\times n$ antisymmetric adjoint matrix representation for the commutation operation $[-iH,\cdot\,]$. All the parameters have real values in this representation.

For a two-level system we have $n=2$, and we can assume a single vector direction $\vec{a}$ for both the field $\vec{E}$ and the polarization $\vec{P}$, reducing these quantities to scalars. With $\hat{Q} = Q\vec{a}$, we the have the explicit representations

$$\hat{H}_0 = -\frac{\hbar\omega_0}{2}\begin{pmatrix} 1 & 0 \\ 0 & -1 \end{pmatrix}, \tag{6a}$$

$$Q=q_0\begin{pmatrix}0 & 1\\ 1 & 0\end{pmatrix}, \tag{6b}$$

where ω_0 is the atomic transition resonance frequency from the ground level to the excited level. The constant q_0 is an atomic length scale having a typical physical magnitude $q_0=10^{-10}m$. The nonlinear differential system (5) and (6) reduces to

$$\partial_t\begin{pmatrix}\rho_1\\ \rho_2\\ \rho_3\end{pmatrix}=\begin{pmatrix}0 & \omega_0 & 0\\ -\omega_0 & 0 & 2\Omega_R\\ 0 & -2\Omega_R & 0\end{pmatrix}\begin{pmatrix}\rho_1\\ \rho_2\\ \rho_3\end{pmatrix} \tag{7}$$

where, if the dipole coupling coefficient $\gamma=eq_0$, the Rabi frequency

$$\Omega_R=\frac{\gamma}{\hbar}E. \tag{8}$$

The terms ρ_1, ρ_2, and ρ_3 satisfy the relationship $\rho_1^2+\rho_2^2+\rho_3^2=1$ and represent, respectively, the dispersive or in-phase component of the polarization, the absorptive or in-quadrature component of the polarization, and the fractional difference in the populations for the two energy levels. The near-resonant behavior of nonlinear systems cannot be meaningfully discussed unless dissipative effects are taken into account. The usual method of achieving this in simple systems is to include phenomenologically obtained diagonal terms consisting of characteristic decay rates in the Liouville equation (7). In particular, we have

$$\partial_t\begin{pmatrix}\rho_1\\ \rho_2\\ \rho_3\end{pmatrix}=\begin{pmatrix}0 & \omega_0 & 0\\ -\omega_0 & 0 & 2\Omega_R\\ 0 & -2\Omega_R & 0\end{pmatrix}\begin{pmatrix}\rho_1\\ \rho_2\\ \rho_3\end{pmatrix}-\begin{pmatrix}\frac{1}{T_2} & 0 & 0\\ 0 & \frac{1}{T_2} & 0\\ 0 & 0 & \frac{1}{T_1}\end{pmatrix}\begin{pmatrix}\rho_1\\ \rho_2\\ \rho_3-\rho_{30}\end{pmatrix}, \tag{9}$$

where T_1 is the excited-state lifetime, T_2 is the dephasing time, and ρ_{30} is the initial population difference in the system. Note that the specification that $\rho_{30}=-1$ represents all the atoms initially being in their ground states.

We take the incident electromagnetic field to be a uniform plane wave that is propagating along the z axis and is polarized along the x axis; i.e., $\vec{E}(\vec{r},t)=E_x(z,t)\hat{\vec{x}}$ and $\vec{H}(\vec{r},t)=H_y(z,t)\hat{\vec{y}}$. Thus the spatial orientation of the dipole is $\vec{a}=\hat{\vec{x}}$. This means the polarization is $\vec{P}=P_x\hat{\vec{x}}$, where

$$P_x(t)=-N_{\text{atom}}\gamma\rho_1(t). \tag{10}$$

The one-dimensional Maxwell-Bloch system resulting from this reduction of Eqs. (1) and (9) is thus as follows.

Maxwell equations.

$$\partial_t H_y=-\frac{1}{\mu_0}\partial_z E_x, \tag{11a}$$

$$\partial_t E_x=-\frac{1}{\epsilon_0}\partial_z H_y-\frac{1}{\epsilon_0}\partial_t P_x=-\frac{1}{\epsilon_0}\partial_z H_y-\frac{N_{\text{atom}}\gamma}{\epsilon_0 T_2}\rho_1+\frac{N_{\text{atom}}\gamma\omega_0}{\epsilon_0}\rho_2. \tag{11b}$$

Bloch equations.

$$\partial_t\rho_1=-\frac{1}{T_2}\rho_1+\omega_0\rho_2, \tag{12a}$$

$$\partial_t\rho_2=-\omega_0\rho_1-\frac{1}{T_2}\rho_2+2\frac{\gamma}{\hbar}E_x\rho_3, \tag{12b}$$

$$\partial_t\rho_3=-2\frac{\gamma}{\hbar}E_x\rho_2-\frac{1}{T_1}(\rho_3-\rho_{30}). \tag{12c}$$

This system of equations can be discretized using finite differences in several different ways. The approach we have developed to date to be the most efficient and well-behaved numerical algorithm is based upon a predictor-corrector iterative scheme; it is discussed in detail in the Appendix. This approach allows solution of all of the equations in the system with each time update.

We note that the rotating-wave approximation (RWA) has been used effectively to describe self-induced transparency effects in a two-level atom. There are many examples of SIT studies [12–21]. Our system of equations agrees with Eilbeck and Bullough's system [17] when $\rho_1\rightarrow+r_1$, $\rho_2\rightarrow-r_2$, $\rho_3\rightarrow+r_3$, and $\gamma\rightarrow-p$. Their ground state $\rho_3=-1$ corresponds to our specification that $\rho_{30}=-1$. In terms of the density-of-states matrix $\hat{\rho}_{mn}$ discussed by Yariv in [20], we have $\rho_1=\hat{\rho}_{12}+\hat{\rho}_{21}=2\,\text{Re}\{\hat{\rho}_{12}\}$, $\rho_2=i(\hat{\rho}_{12}-\hat{\rho}_{21})=-2\,\text{Im}\{\hat{\rho}_{12}\}=+2\,\text{Im}\{\hat{\rho}_{21}\}$, and $\rho_3=\hat{\rho}_{22}-\hat{\rho}_{11}$. We have chosen the present form (9) primarily to maintain real number for all the quantities throughout the numerical simulations.

The steady-state nature of the nonlinear behavior obtained from this system can be characterized as follows. Since $P_x=-N_{\text{atom}}\gamma\rho_1=\epsilon_0\chi E_x$, the index of refraction satisfies the relation

$$n^2=1+\chi=1-\frac{N_{\text{atom}}\gamma\rho_1}{\epsilon_0 E_x}.$$

Consider the case of equilibrium for a slowly varying pulse in the absence of loss, so that we can assume that $E_x\sim E_{\text{eq}}=\text{const}$. Then $0=\omega_0\rho_2^{\text{eq}}$ and $0=-\omega_0\rho_1^{\text{eq}}+\Omega_R^{\text{eq}}\rho_3^{\text{eq}}$, so that $\rho_2^{\text{eq}}=0$ and $\rho_3^{\text{eq}}=(\omega_0/\Omega_R^{\text{eq}})\rho_1^{\text{eq}}$. Therefore, with $\rho_1^2+\rho_2^2+\rho_3^2=\rho_3^2[1+(\Omega_R^{\text{eq}}/\omega_0)^2]=1$ and $(\Omega_R^{\text{eq}}/\omega_0)^2\ll 1$, we obtain

$$n^2 = 1 - \frac{N_{\text{atom}}\,\gamma}{\epsilon_0 E_{\text{eq}}}(\Omega_R^{\text{eq}}/\omega_0)\rho_3^{\text{eq}}$$
$$= 1 - \frac{N_{\text{atom}}\,\gamma^2}{\epsilon_0(\hbar\omega_0)}[1+(\Omega_R^{\text{eq}}/\omega_0)^2]^{-1/2}$$
$$\approx 1 - \frac{N_{\text{atom}}\,\gamma^2}{\epsilon_0(\hbar\omega_0)} + \frac{N_{\text{atom}}\,\gamma^4}{2\epsilon_0(\hbar\omega_0)^2}E_{\text{eq}}^2, \tag{13}$$

which shows that the index of refraction is dependent on the square of the equilibrium electric-field value. Thus the two-level atom has Kerr-medium characteristics when equilibrium is reached.

On the other hand, for an extremely short pulse in which $T_p \ll T_1, T_2$, we must investigate the transient behavior of the system. In particular, we are interested in the impact of the time derivative of this pulse on the behavior of the two-level system. When $T_p \ll T_1, T_2$, one has from Eqs. (11) and (12) that

$$\partial_t E_x \approx -\frac{1}{\epsilon_0}\partial_z H_y + \left(\frac{N_{\text{atom}}\,\gamma\omega_0}{\epsilon_0}\right)\rho_2, \tag{14a}$$

$$\partial_t^2\rho_1 + \omega_0^2\rho_1 \approx \left(\frac{2\gamma}{\hbar}\right)E_x\rho_3, \tag{14b}$$

$$\partial_t^2\rho_2 + \left[\omega_0^2 + \left(\frac{2\gamma}{\hbar}E_x\right)^2\right]\rho_2 \approx +\left(\frac{2\gamma}{\hbar}\right)\rho_3\partial_t E_x, \tag{14c}$$

$$\partial_t^2\rho_3 + \left(\frac{2\gamma}{\hbar}E_x\right)^2\rho_3 \approx \left(\frac{2\gamma}{\hbar}\right)[\omega_0\rho_1 E_x - \rho_2\partial_t E_x]. \tag{14d}$$

It is evident that the nonlinear behavior is dependent not only on the electric field E_x, but also on its time derivative $\partial_t E_x$. As discussed in Refs. [26–29], contributions to the polarization of the medium from time-derivative behaviors are known to occur even in linear media. The relations (14a)–(14d) indicate that when $E_x \sim 0$ and $\partial_t E_x \neq 0$ the time-derivative terms completely dominate the evolution of the nonlinear two-level system. In particular, when $E_x \sim 0$ the rate equation (12c) yields $\partial_t\rho_3 = 0$ and the oscillator equations (14b)–(14d) give

$$\partial_t^2\rho_1 + \omega_0^2\rho_1 \sim 0, \tag{15a}$$

$$\partial_t^2\rho_2 + \omega_0^2\rho_2 \sim \frac{2\gamma}{\hbar}\rho_3\partial_t E_x, \tag{15b}$$

$$\partial_t^2\rho_3 \sim -\frac{2\gamma}{\hbar}\rho_2\partial_t E_x. \tag{15c}$$

Together with (12c), Eq. (15c) means that ρ_3 should act like a cubic function near the points where $E_x \sim 0$ and should be asymmetric in value with respect to those points. Moreover, Eqs. (15b) and (15c) show that the time-derivative behavior will sustain the nonlinear process through these null-field points. Finally, when both E_x and $\partial_t E_x$ are zero (after the pulse has passed through a region of two-level atoms), we find from Eqs. (15a)–(15c) that the ρ_1 and ρ_2 terms oscillate at the level frequency ω_0 and that the level density ρ_3 becomes a constant; i.e., $\partial_t^2\rho_3 \sim 0$ from Eq. (14d) and $\partial_t\rho_3 \sim 0$ from Eq. (12c). Note that if a second pulse were to interact with the resulting two-level atom medium it would have to propagate in the presence of these oscillating ρ_1 and ρ_2 terms.

Finally, the FDTD Maxwell-Bloch simulator can also recover standard small-signal gain conditions. This will allow eventual investigations of ultrafast-pulse propagation in amplifiers and microcavity lasers. The small-signal gain coefficient can be obtained from a RWA of the Maxwell-Bloch system. In particular, in the limit $\omega_0 T_2 \gg 1$ and $\omega_{\text{Rabi}} \ll \omega_0$, where the Rabi radial frequency

$$\omega_{\text{Rabi}} = \frac{\gamma E_0}{\hbar}, \tag{16}$$

consider the time derivatives of Eqs. (11a) and (12a). These yield the relations

$$\partial_{ct}^2 E_x - \partial_z^2 E_x = N_{\text{atom}}\,\gamma\mu_0\left\{-\omega_0^2\rho_1\left[1 - \frac{1}{(\omega_0 T_2)^2}\right] - 2\frac{\omega_0}{T_2}\rho_2 + 2\frac{\gamma}{\hbar}E_x\omega_0\rho_3\right\} \tag{17a}$$
$$\approx -N_{\text{atom}}\,\gamma\mu_0\omega_0^2\rho_1\left[1 - \frac{1}{(\omega_0 T_2)^2}\right]$$
$$\sim -N_{\text{atom}}\,\gamma\mu_0\omega_0^2\rho_1,$$

$$\partial_t^2\rho_1 + \frac{1}{T_2}\partial_{ct}\rho_1 + \omega_0^2\rho_1 = 2\frac{\gamma}{\hbar}E_x\omega_0\rho_3 - \frac{\omega_0}{T_2}\rho_2$$
$$\approx 2\frac{\gamma}{\hbar}E_x\omega_0\rho_3. \tag{17b}$$

If we make the RWA so that $(E_x, \rho_1, \rho_2) \sim \exp[i(kz-\omega t)](E_0, \rho_{10}, \rho_{20})$ and $\rho_3 \sim \rho_{30}$, we obtain from (17a) and (17b) the expressions

$$\left(-\frac{\omega_0^2}{c^2} + k^2\right)E_0 \sim -N_{\text{atom}}\,\gamma\mu_0\omega_0^2\rho_{10}, \tag{18a}$$

$$\rho_{10} \sim i2\frac{\gamma}{\hbar}E_0 T_2\rho_{30}, \tag{18b}$$

which combine to give the approximate propagation constant

$$k^2 \sim \frac{\omega_0^2}{c^2}\left[1 - i\left(\frac{2N_{\text{atom}}\,\gamma^2}{\hbar\epsilon_0}\right)T_2\rho_{30}\right], \tag{19}$$

and hence its imaginary part

$$k_{\text{im}} \sim -\rho_{30}\left(\frac{2N_{\text{atom}}\,\gamma^2}{\hbar\epsilon_0}\right)\frac{\omega_0 T_2}{c} \equiv -\rho_{30}\,g. \tag{20}$$

The resulting small-signal gain coefficient g, which occurs when $\rho_{30} = +1$, agrees with known expressions [see, for instance, Ref. [25], Eq. (8.5.14)]. Of course, the FDTD Maxwell-Bloch simulator will contain all of the dynamics including those associated with the RWA. As will be shown below, the initial conditions can be arranged in an essentially

sinusoidal input-signal configuration to test the recovery of the expected small-signal gain $\exp(gL)$ in the electric field or the corresponding intensity gain $\exp(2gL)$, where L is the length of the gain medium. Moreover, the simulator allows one to explore the behavior of a gain medium in a variety of other pulse configurations. We note that, in contrast to Hawkins and Kallman's approach [30], which incorporates gain in the FDTD approach by treating the gain medium as a phenomenological negative-conductivity region, our FDTD Maxwell-Bloch simulator results can be connected directly to the parameters associated with the two-level atoms.

III. NUMERICAL RESULTS

We will first compare the FDTD SIT results with those obtained from the approximate RWA analytical arguments. In particular, it is known (e.g., [21]), that the pulse

$$E_x(z,t)=\tilde{E}_x(z,t)\sin(\omega t), \tag{21}$$

which has as its envelope

$$\tilde{E}_x(z,t)=E_0\ \mathrm{sech}[(t-z/v)/\tau_p], \tag{22}$$

will produce SIT results if that envelope $\tilde{E}_x$ has a pulse area

$$A_{\mathrm{pulse}}=\int_{-\infty}^{\infty}\frac{\gamma}{\hbar}\tilde{E}_x(t')dt'=\frac{\gamma}{\hbar}E_0\int_{-\infty}^{\infty}\mathrm{sech}\,(t'/\tau_p)dt'$$

$$=\frac{\gamma E_0}{\hbar}\tau_p\pi \tag{23}$$

that is an integer multiple of 2π. The constant $\hbar=h/(2\pi)=1.0546\times10^{-34}$. A 2π pulse gives a complete transition of the two-level system from its ground state to its excited state and back to its ground state while maintaining the shape of the excitation pulse. This transition occurs in one Rabi period $T_{\mathrm{Rabi}}=2\pi/\omega_{\mathrm{Rabi}}$. Thus we can rewrite the envelope pulse area as

$$\frac{A_{\mathrm{pulse}}}{2\pi}=\frac{\gamma E_0}{2\hbar}\tau_p=\frac{\omega_{\mathrm{Rabi}}\tau_p}{2}. \tag{24}$$

For all of the SIT simulations discussed below, we begin the pulse propagating into the FDTD mesh at the left boundary (which is identified with $z=0$) with the initial time history

$$E_x(z=0,t)=E_0\ \mathrm{sech}\,(10\Gamma)\ \sin\,(\omega,t), \tag{25}$$

where $\Gamma=[t-(T_p/2)]/(T_p/2)$, T_p being the pulse duration. Comparing with (22), the constant $\tau=T_p/20$. We take the carrier frequency to be equal to the chosen level transition frequency, $\omega=\omega_0=2\pi f_0$, $f_0=2.0\times10^{14}\ \mathrm{s}^{-1}$. The pulse duration is finite and set equal to $T_p=20T_0=20/f_0=100.0$ fs. With (22) and (25) this means that we have chosen $\tau=1/f_0$. Consequently, if the coupling coefficient $\gamma=1.0\times10^{-29}$, the amplitude of the SIT pulse (21) necessary to achieve a specified pulse area is

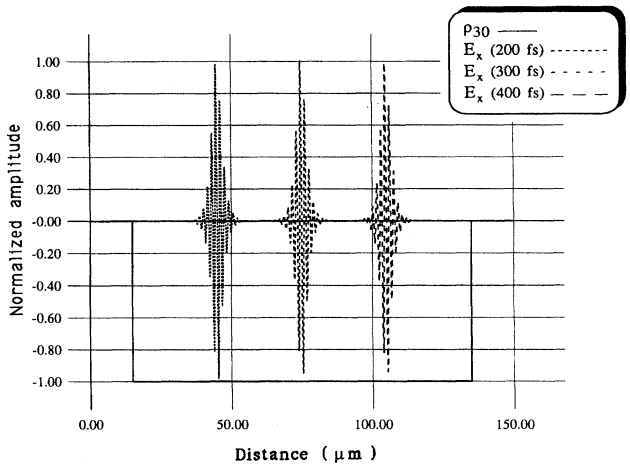

FIG. 1. For the SIT 2π pulse the electric field propagates as a solitary wave in the two-level atom medium. All of the atoms are taken to be initially in the ground state; this corresponds to the initial population profile $\rho_{30}=-1$ as shown in this figure. The simulation region is 150 μm long; the two-level atom medium extends from 7.5 to 142.5 μm. The normalized (to $E_{\max}$) electric-field profiles [E_x(200 fs), E_x(300 fs), and E_x (400 fs)] at the simulation times $t=200$, 300, and 400 fs are shown.

$$E_0=\frac{\hbar A_{\mathrm{pulse}}}{\gamma\tau_p\pi}\frac{1}{\arctan\,(\sinh u)\big|_{-10}^{+10}}=\frac{2\hbar f_0}{0.999\,942\gamma\pi}\frac{A_{\mathrm{pulse}}}{2\pi}$$

$$=4.2186\times10^9\frac{A_{\mathrm{pulse}}}{2\pi}. \tag{26}$$

Therefore a 2π pulse requires a maximum electric-field amplitude $E_0=4.2186\times10^9$.

The simulation region is taken to be N_{cells} cells long. The pulse initially propagates in a free-space region, then enters the two-level atom medium for a specified distance, and finally exits the medium into another free-space region. For all of the simulations noted below, the number of atoms in the two-level medium is set equal to $N_{\mathrm{atoms}}=10^{24}\ \mathrm{m}^{-3}$. The cell size $\Delta z=\lambda_0/200=7.5$ nm was chosen to ensure very accurate numerical results. The resulting time step is set equal to half the Courant-condition value; i.e., $\Delta t=0.5\times\Delta z/c=1.25\times10^{-17}$ s, where $c=3.0\times10^8$ m/s is the speed of light, the speed of the signals in the free-space region. In order to meet the SIT criterion that $T_1, T_2\gg T_p$, we have set $T_1=T_2=1.0\times10^{-10}$.

With the indicated parameter choices, the 2π-pulse simulations essentially recover the known analytical results. The 2π-pulse simulation region was taken to be 150.0 μm or $N_{\mathrm{cells}}=20\,000$ long. The left and right free-space regions are 7.5 μm wide. The two-level atom medium is 135.0 μm long. A $T_p=20T_0$ pulse in free space is 30.0 μm long spatially. The numerically predicted electric-field profiles E_x for the simulation times $t=200.0$, 300.0, and 400.0 fs are shown in Fig. 1. Also plotted in this figure is the initial ground-state distribution of ρ_3, i.e., $\rho_3=\rho_{30}=-1$. It is clear from this figure that the SIT electric field propagates as though it were unaffected by the presence of the nonlinear medium, i.e., as a solitary wave. A closer look at the electric field and the ρ_3

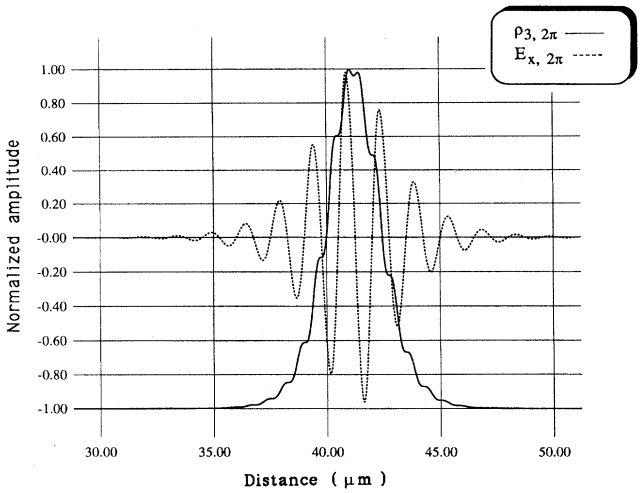

FIG. 2. The SIT 2π pulse completely excites and deexcites the two-level atom medium locally. The normalized electric-field ($E_{x,2\pi}$) and population ($\rho_{3,2\pi}$) profiles are given for the simulation time $t=187.5$ fs in the region 25.0–55.0 μm. The flattenings of the population profile where the time derivative of the electric field is maximum or minimum are apparent.

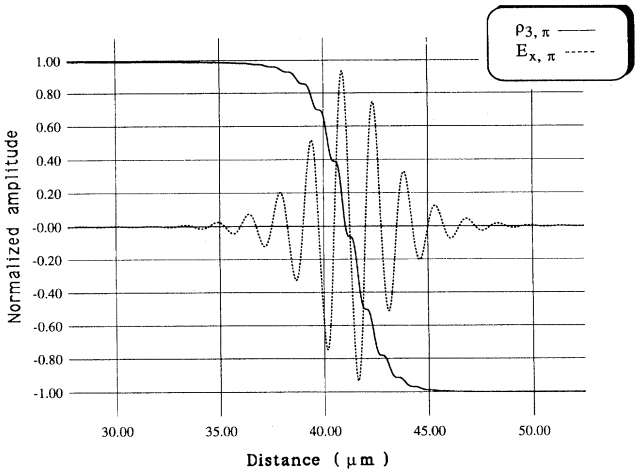

FIG. 3. The SIT π pulse completely excites the two-level atom medium locally. The normalized electric-field ($E_{x,\pi}$) and population ($\rho_{3,\pi}$) profiles are given for the simulation time $t=187.5$ fs in the region 25.0–55.0 μm. The flattenings of the population profile where the time derivative of the electric field is maximum or minimum are apparent.

profiles at $t=187.5$ fs is given in Fig. 2. This agrees with the known analytical results *except* for the additional cubic polynomial-like features that appear in the ρ_3 profiles. The medium is completely inverted by the leading edge of the electric-field pulse; the two-level atoms then decay by stimulated emission back to their ground state, giving the original excitation energy back to the pulse. The cubic-polynomial features occur at the null-field points of the pulse as expected from the transient analysis of the preceding section. The transitions between the ground and excited levels represented by ρ_3 begin to slow and may even be reversed locally at these null-field points by the time-derivative behavior of the field. We note that any 2ω effects, which are absent in the RWA, would also manifest themselves at these points. The single-cycle-pulse cases introduced below substantiate the conclusion that these features are associated with the time-derivative behavior.

Also considered were the π-pulse and 4π-pulse excitations. The resulting electric-field and ρ_3 profiles for these cases are shown in Figs. 3 and 4, respectively. The maximum electric-field value for these two cases is, respectively, $E_0^{\pi}=\frac{1}{2}E_0^{2\pi}=2.1093\times10^9$ and $E_0^{4\pi}=2E_0^{2\pi}=8.4372\times10^9$. As known from analytical results, the π pulse completely inverts the medium. Similarly, the 4π pulse shows the expected two symmetrical transversals between the ground and excited states. However, in all cases the null-field, time-derivative features are present.

In order to emphasize these transient features further, we have also investigated the response of the two-level atom to ultrafast pulses which have no carrier. Such a pulse could be, for example, a single cycle of the multiple-cycle 2π pulse. Originally, it was expected that we would see little to no effect from these pulses since there was little energy at the transition frequency in such a broad-bandwidth excitation. Moreover, it was also expected that any significant changes in the medium's properties would occur only after a time span greater than several cycles. The results were quite surprising. It was found that the state of the two-level atom medium could be completely controlled instantaneously with the ultrafast pulses in a fashion similar to the carrier response.

Because the single-cycle sinusoid has a discontinuous derivative at its end points, a great deal of numerical noise was generated in those original simulations. To probe the medium more effectively, we have used the excitation pulse

$$E_x(z=0,t)=E_0\,f(t), \tag{27}$$

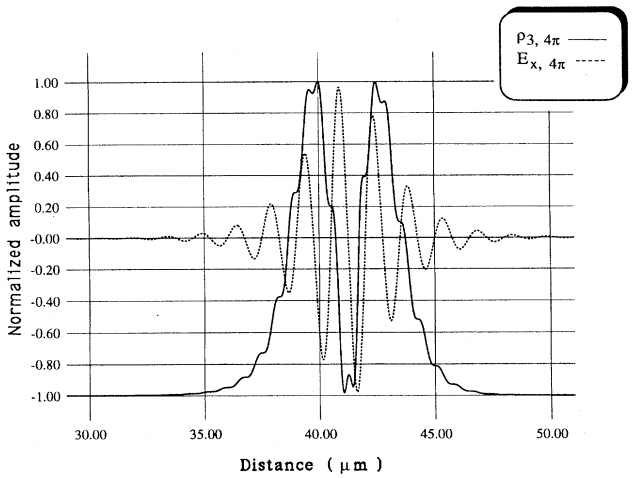

FIG. 4. The SIT 4π pulse completely twice excites and deexcites the two-level atom medium locally. The normalized electric-field ($E_{x,4\pi}$) and population ($\rho_{3,4\pi}$) profiles are given for the simulation time $t=187.5$ fs in the region 25.0–55.0 μm. The flattenings of the population profile where the time derivative of the electric field is maximum or minimum are apparent.

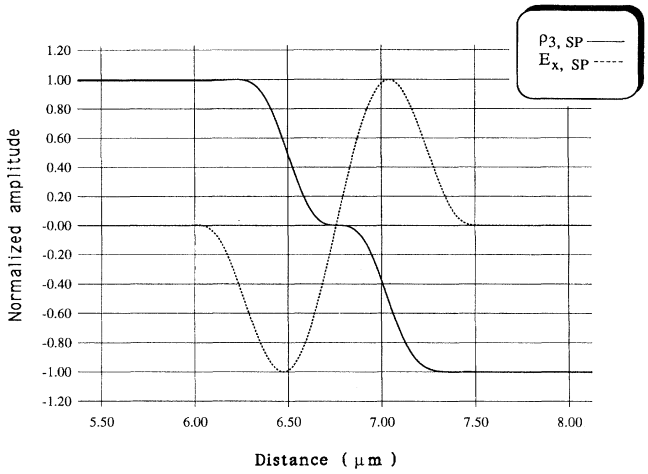

FIG. 5. A designed ultrafast pulse can completely excite the two-level atom medium locally. The normalized electric field ($E_{x,\mathrm{SP}}$) and population ($\rho_{3,\mathrm{SP}}$) profiles are given for the simulation time $t=12.5$ fs in the region 5.5-8.0 μm. The flattening of the population profile where the time derivative of the electric field is maximum is apparent.

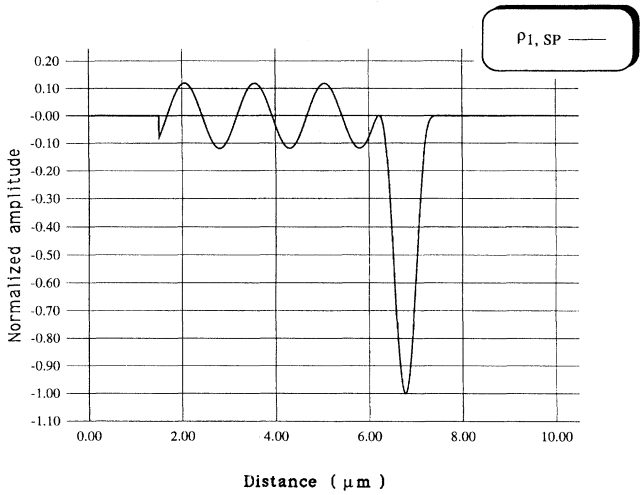

FIG. 6. The ρ_1 profile corresponding to the ultrafast-pulse case shown in Fig. 5 is given. After the initial variations due to the pulse, the medium settles into oscillations at the resonance frequency of the excited state.

where the time signal

$$f(t)=\begin{cases} 0 \quad \text{for} \quad t<0 \\ -4.201\,355x(1-x^2)^3 \quad \text{for} \quad 0\leq t\leq T_p \\ 0 \quad \text{for} \quad t>T_p \end{cases} \tag{28}$$

and the term $x=(2T/T_p)-1$. This pulse has continuity in its first two derivatives at all points; it is a bipolar pulse which has zero area. To localize the spectrum of this broad-bandwidth pulse about the transition frequency f_0, the total pulse width is set equal to the width of one cycle of the sinusoid in (21); i.e., $T_p=5.0$ fs. The maximum of the spectrum of (27) then occurs at f_0. This pulse propagates through the two-level atom medium with only minuscule changes. However, it has a profound impact on the state of the atoms.

Because the pulse (27) with $T_p=5.0$ fs is much smaller in length (1.5 μm) than the SIT pulses (30.0 μm), the simulation region for these ultrafast-pulse cases was taken to be only $N_{\mathrm{cells}}=2000$ or 15.0 μm in length. The resulting electric-field and ρ_3 profiles for the short-pulse (27) excitation with $E_0=8.205\times10^9$ at the simulation time $t=12.5$ fs are shown in Fig. 5. The corresponding ρ_1 and ρ_2 profiles at the same time are given in Figs. 6 and 7, respectively. This choice of E_0 was engineered to cause the cubic feature to occur at the null-field point crossing of the electric field. A larger (smaller) value of E_0 causes this feature to occur at positive (negative) ρ_3 values. This pulse has completely inverted the two-level system, despite the pulse area being zero and the frequency content at f_0 being only a small portion of the total energy content of the pulse. In contrast to the SIT pulse which might be classified as resulting from an integrated effect over the entire wave form, the present result occurs because the time derivative has a large instantaneous value. This is immediately confirmed by comparing the E_x, ρ_1, and ρ_2 profiles directly when the E_x field is nonzero. One finds that ρ_2 follows E_x instantaneously so that the peak in ρ_1 occurs at the peak in $\partial_t E_x$. The shape of ρ_1 coincides over this interval in time with the behavior of $\partial_t E_x$ between its two minima. In Figs. 6 and 7 note that once the pulse has turned off both ρ_1 and ρ_2 oscillate at the transition frequency f_0 as predicted by Eqs. (14b) and (14c). Also note that with the indicated choices for T_1 and T_2 the lifetime of the inverted state is approximately $10^4 T_p$.

We have also considered using the same pulse shape to cause, like the 4π SIT pulse, two transitions between the ground and excited states during T_p. This possibility was explored by simply increasing the magnitude of the time signal exciting the two-level system. The best behavior we found is shown in Fig. 8 in which the electric-field and ρ_3 profiles for the short-pulse (27) excitation with $E_0=2.272\times10^{10}$ at the simulation time $t=12.5$ fs are given. It was found that it is not possible to achieve two complete symmetric inversions with only the time signal (27). We were only able to obtain about a 70% inversion in each swing of the pulse. This is due to the derivative nature of the effect. The medium is responding rapidly to the variations in the pulse shape and its time derivative. A pulse would have to be designed which incorporated two derivative maxima to achieve the desired effect.

These single-pulse results indicate that it may be possible to achieve multiple inversions if enough time were provided so that a single pulse could achieve the first inversion and a later pulse of the same form could be used to achieve the next inversion, and so on. To test this possibility, we considered the excitation $E_x(z=0,t)=E_0[f(t)+\alpha f(t-mT_p)]$, where $\alpha=0.96$ and $m=3$. The simulation region was increased to $N_{\mathrm{cells}}=5000$ to accommodate the larger overall pulse length. The resulting electric-field and ρ_3 profiles for the excitation with $E_0=8.235\times10^9$ at the simulation time $t=62.5$ fs are shown in Fig. 9. The leading pulse completely inverts the two-level atom medium; the second pulse then completely deexcites it. The need for the amplitude of the

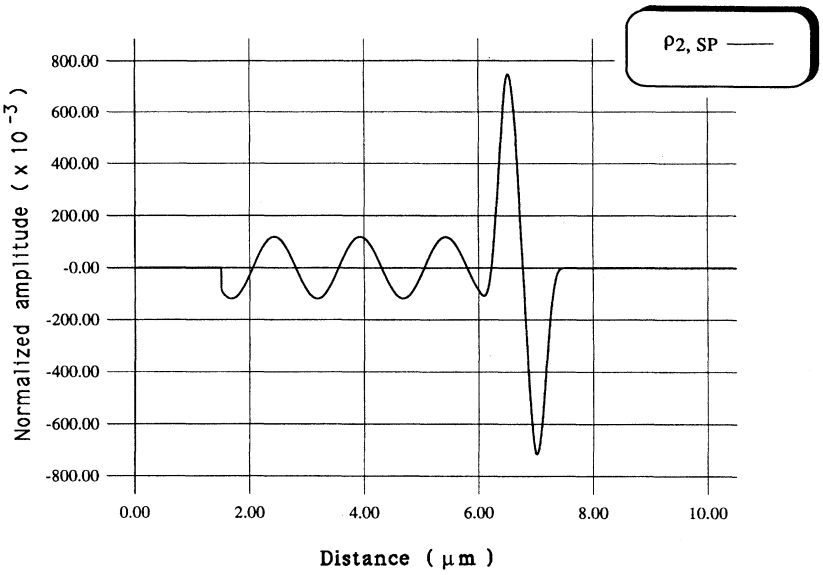

FIG. 7. The ρ_2 profile corresponding to the ultrafast-pulse case shown in Fig. 5 is given. After the initial variations due to the pulse, the medium settles into oscillations at the resonance frequency of the excited state.

second pulse to be slightly lower than the original value results from the medium still having energy residing in ρ_1 and ρ_2, which were set into oscillation at f_0 with small amplitudes by the initial pulse. This has been tested with a longer set of these pulses with the result that one can control the final state of the two-level atom medium with an engineered sequence of pulses.

For the gain validation case we considered an initial pulse (27) which has a unit amplitude, $E_0=1.0$, and the time signal

$$g(t)=\sin(\omega_0 t)\times\begin{cases}0 & \text{for } t<0\\ (1-x^2)^4 & \text{for } 0\leq t\leq 5T_p\\ 1 & \text{for } t>5T_p,\end{cases} \quad (29)$$

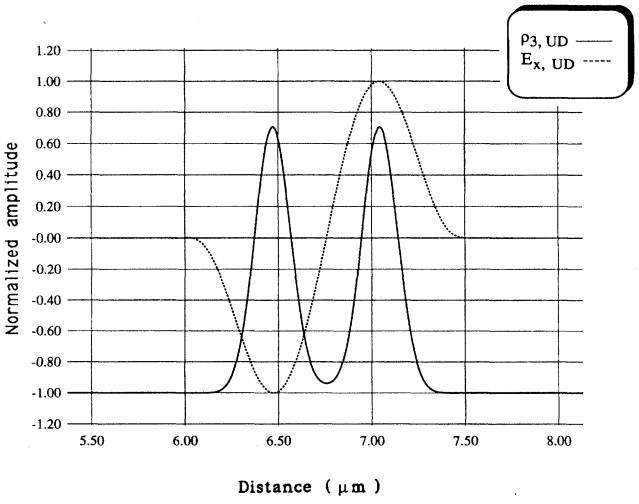

FIG. 8. A designed ultrafast pulse can excite and deexcite the two-level atom medium locally. The normalized electric field ($E_{x,\mathrm{UD}}$) and population ($\rho_{e,\mathrm{UD}}$) profiles are given for the simulation time $t=12.5$ fs in the region 5.5–8.0 μm. The flattenings of the population profile where the time derivatives of the electric field are maximum or minimum are apparent.

where the term $x=(2T/T_p)-1$. This represents a continuous-wave sinusoid at the transition frequency after a smooth turn-on over 5 periods. The simulation space was shortened to $N_{\mathrm{cells}}=2000$ or 15.0 μm to accommodate the larger number of time steps (150 000) that were run, and hence the associated data storage and simulation costs. The number of atoms and the coupling constant were held fixed at $N_{\mathrm{atom}}=1.0\times10^{24}$ and $\gamma=1.0\times10^{-29}$. The length of the two-level atom medium was fixed at $L=9.0$ μm. The medium was assumed to be initially in its inverted state so that $\rho_{30}=+1.0$; this provides the appropriate initial conditions for gain to occur. The time constants were set to $T_1=1.0\times10^{-10}$ s and $T_2=5.0\times10^{-14}$ s. This gives the frequency–relaxation-time product $f_0T_2=10.0$ or $\omega_0T_2=62.8$, which satisfies the condition that led to the small signal-gain coefficient (20). The smaller (than previously assumed) value for T_2 was chosen for two reasons. First, the gain coefficient is small: $g=0.0225$ $\mu\mathrm{m}^{-1}$; and secondly the time for saturation effects to occur is reasonable: $10T_2=500.0$ fs which corresponds to 40000 time steps. Thus with 150 000 time steps the simulation is well into the saturation region. The unit-amplitude initial electric field is so small that the gain medium is only minutely perturbed by the presence of the pulse. The expected amplitude and intensity gains away from the saturation region are, respectively, $\exp(gL)=1.224$ and $\exp(2gL)=1.498$. In the saturation region the gain coefficient becomes half of its peak value [31]; hence the gain values become $\exp(gL/2)=1.1064$ and $\exp(gL)=1.224$ respectively.

The intensity of the electric field was measured as a function of time at ten cells before and after the medium. Only every tenth time value was collected since the data manipulation become prohibitive with the available computer platform. The envelopes of the normalized intensities at these points are compared in Fig. 10. The solid (dotted) line represents the normalized intensity values after (before) the medium. Gain is evident as is the switch to saturation which occurs in time at $10T_2$ after the output field has reached the observation point. The peak value of the gain is 1.483 and the saturation value is 1.223. These results are in reasonable

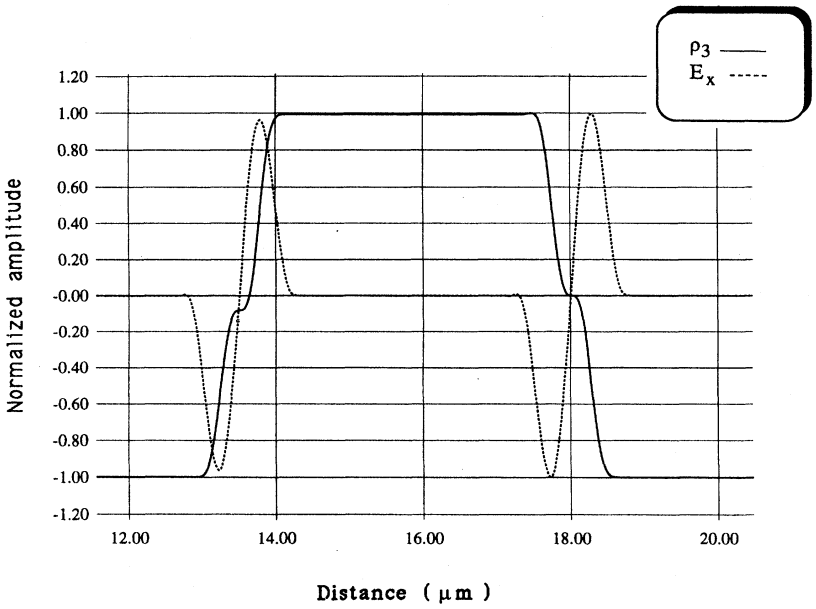

FIG. 9. An ultrafast-pulse train can be designed to excite the two-level atom medium locally and then deexcite it at a desired, later time. The normalized electric-field (E_x) and population (ρ_3) profiles are given for the simulation time $t=62.5$ fs in the region 12.0–20.0 μm. The flattenings of the population profile where the time derivatives of the electric field are maximum or minimum are apparent.

agreement with the analytical values; the slight discrepancy between the peak value and the expected one is attributed to the slight loss in resolution associated with our restricted data set. A plot of the electric field everywhere in the simulation region at the final time step is given in Fig. 11. The electric field (dotted line) is superimposed on the initial values of ρ_3. Notice the unit-amplitude field before the medium, the gain of the field in the medium, and the steady-state field value after the medium. The final maximum electric-field value is 1.1063, corresponding to the expected value of 1.1064.

Another potential application for the ultrafast inversion pulse discussed above is to pump the two-level medium to provide a gain medium for a trailing probe pulse. This possibility was also explored with the simulator. Because of the anticipated large variations between the pump and the probe, the discretization was increased to $\lambda_0/400$ and the number of cells was increased to 4000 to keep the simulation space the same length, 15.0 μm; the length of the two-level atom medium was also held constant at 9.0 μm. The time relaxation parameters were fixed to match the sinusoid gain case, i.e., $T_1=1.0\times10^{-10}$ s and $T_2=5.0\times10^{-14}$ s. The incident pulse for this simulation was $E_x(z=0,t)=E_{\max}[f(t)+\beta g(t-T_{\text{delay}})]$, where $E_{\max}=8.232\times10^9$. The slightly different value of $E_{\max}$ from the previous single- and multiple-ultrafast-pulse cases result from the differences in the values for T_2. Moreover, in contrast to those cases, it was found that the ultrafast pump pulse with $T_2 \ll T_1$ only inverts approximately 95% of the two-level atoms. The choices of β and T_{delay} in the incident pulse also significantly

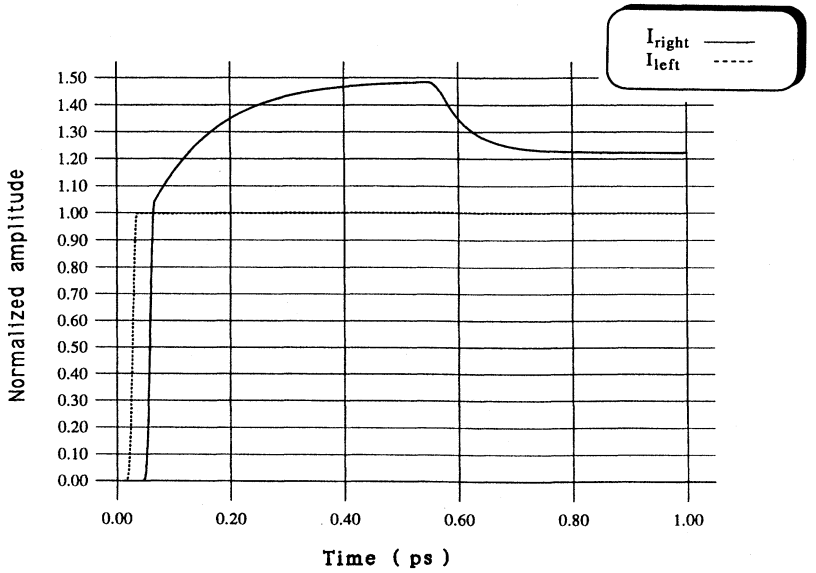

FIG. 10. The FDTD Maxwell-Bloch simulator can also recover small-signal gain results. The envelope of the normalized output intensity measured just after the gain medium (I_{right}) is compared with the corresponding input intensity envelope measured just before it (I_{left}).

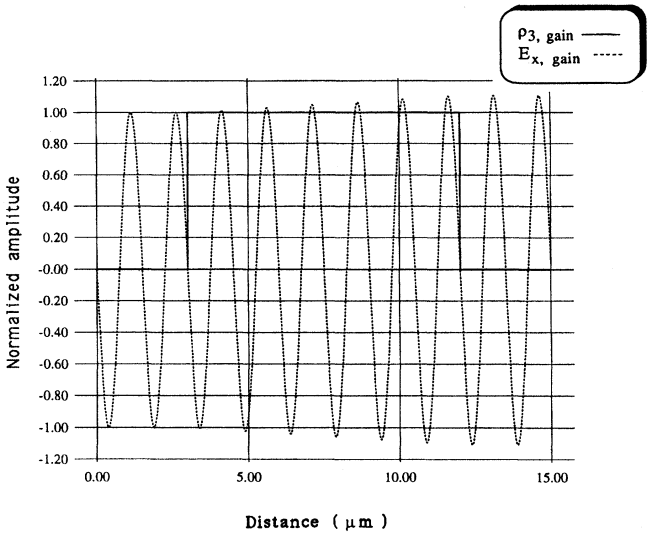

FIG. 11. The small-signal electric field ($E_{x,\text{gain}}$) at every point in the simulation region at the time 1.875 ps is plotted against the initial ρ_3 distribution ($\rho_{3,\text{gain}}$).

impact the results. It was found that β must be a small number to avoid depleting the number of atoms in the inverted state. Even a value of $\beta=0.01$ caused the medium to relax at late times to a state with $\rho_3 \sim 0.0$ yielding very little gain. A peak gain of the output signal relative to the input probe signal intensity of 1.1615 was obtained at earlier times. The amplitude was then scaled down to $\beta=1.0\times10^{-4}$. Although some perturbations of the late-time ρ_3 values continued, the results were much closer to the undepleted, sinusoidal-pump case.

The delay time between the pump and probe pulses, T_{delay}, affects what kind of medium the probe pulse experiences. The longer the delay, the more time the two-level atom medium has to relax into its equilibrium state. For instance, with the indicated T_1 and T_2 values, the ρ_1 and ρ_2 parameters have an e-folding time T_2 which is much larger than the pump-pulse on time T_p. However, if $T_{\text{delay}}=3.0T_p$ as it was in the ultrafast-pulse multiple-inversion case, the small-amplitude probe pulse will experience a strongly perturbed medium with very large values of ρ_1 and ρ_2. It was found that the system did settle into the saturation regime yielding a small-signal gain value, but the initiation of the probe-pulse effects in the output intensity was not readily observable because the corresponding amplitudes were smaller than the fields arising from the associated relaxation of the medium. However, by increasing the delay time, the system has time to settle. Figure 12 provides a comparison of the envelopes of the normalized input and output intensities at the same locations as the sinusoid gain case for input pulses with $T_{\text{delay}}=20T_p=2.0T_2$ and $T_{\text{delay}}=40T_p=4.0T_2$. It is clearly seen that the input probe pulse experiences different gain conditions depending on the state of the inverted two-level atom medium. Nonetheless, all of the cases relax to the same saturated gain values at late times. The late-time saturated gain value of the intensity is 1.2073, slightly lower than the value obtained in the sinusoid case. This results from the medium having approximately

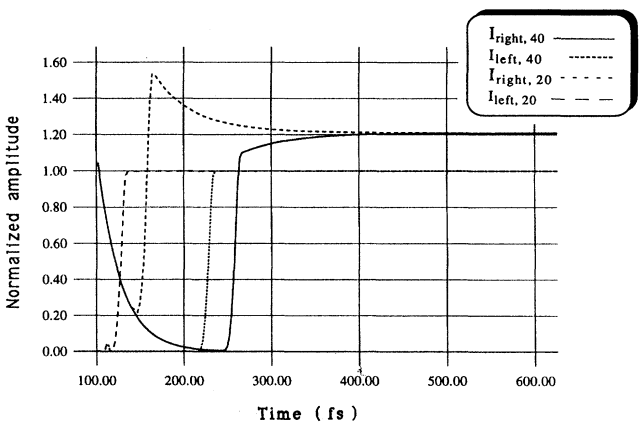

FIG. 12. Using an ultrafast pump pulse, the two-level atom medium can be inverted as shown in Fig. 5. A time-delayed, trailing probe signal will then propagate in the resulting gain medium. The results for this pump-probe configuration are shown. The pump pulse has a time extent of $T_p=5.0$ fs; the probe pulse is a sinusoid at the transition frequency. The envelopes of the normalized output intensity measured just after the gain medium ($I_{\text{right};40}$; $I_{\text{right},20}$) are compared with the corresponding input intensity envelopes measured just before it ($I_{\text{left};40}$; $I_{\text{left},20}$) for probe pulse delays of 40 T_p and $20T_p$.

93.17% of the atoms still in their inverted state at these late times. With $N_{\text{atom}} \rightarrow 0.9317\times N_{\text{atom}}$ in Eq. (20), the saturated gain value of the intensity is 1.2072, very close to the observed result.

IV. CONCLUSIONS

Using a finite-difference time-domain approach to solving the semiclassical Maxwell-Bloch system, we have studied in a more exact manner (without removing the carrier wave) self-induced transparency effects in a two-level atom medium. Standard SIT π, 2π, and 4π results were reproduced. Features appeared at the null-field points and were identified as being associated with the maxima of the time derivative of the electric field. These features are not present in standard approximate solutions to this problem.

These time-derivative effects were emphasized further by considering a variety of ultrafast-pulse cases. It was demonstrated that during ultrafast-pulse interactions with a two-level atom medium a single-cycle pulse can be designed that completely inverts the two-level atom medium. A multiple-pulse train was given that can completely invert the medium from the ground to the excited state and then completely reverse the process. These results confirm that the time-derivative-driven nonlinear properties of the two-level atom medium have a significant impact on the time evolution of this system in the limit of ultrafast pulses.

We also used the FDTD Maxwell-Bloch simulator to recover expected small-signal gain results for sinusoidal input signals. The designed ultrafast inversion pulse was then combined with a sinusoid to form a pump-probe signal set. It was illustrated that a two-level atom medium could be inverted by the leading ultrafast pulse to yield a gain medium for the trailing sinusoidal probe pulse.

Full device and system integration complexities are presently being introduced into our model by considering the multilevel atom (for instance [32], and [33]) and multidimensional (spatial) extensions of the present results. We will be investigating several different amplifier and microcavity laser configurations with the resulting multidimensional FDTD Maxwell-Bloch simulator. These current modeling efforts will be reported in future presentations.

ACKNOWLEDGMENTS

Two of the authors (R.W.Z. and J.M.A) gratefully acknowledge the partial support of this work through the NATO Travel Grant CRG 930312. The authors wish to extend their gratitude to Justin Judkins for his invaluable assistance in developing the numerical scheme used to obtain our results. One of the authors (R.W.Z.) would like to thank Professor Roger Raab for a very enlightening conversation concerning his and Buckingham's original research into the contributions to the polarization vector of a medium from time derivatives of the electric and magnetic fields.

APPENDIX: FDTD SOLUTION OF THE MAXWELL-BLOCH SYSTEM

Practical implementation of the quantum-mechanical Bloch models in large-scale FDTD models of nonlinear electromagnetic devices requires attention to be paid to a number of features, which are now being actively researched. Since the atomic model is computed at every time step for every spatial point, it will form the dominant component of the run time of the code, and must therefore be made very efficient. This is assisted by the form of the equations being first-order differential equations, which means the state variables can be simply updated at each time step from their values at the previous time step. However, practical devices require the tracking of pulses lasting for many optical cycles, over time scales of many pulse widths, implying a very large number of time steps. Under these circumstances, it would be desirable to remove the carrier oscillations explicitly from Eqs. (3) and (4); this is traditionally done by means of the rotating-wave approximation, which is equivalent to a slowly-varying-amplitude approximation, but this becomes progressively more complicated in n-level systems where $n>2$. A better method is Fourier expansion of the field and the density matrix in harmonics of the nominal carrier frequency, with coefficients which are also time dependent, but on a much longer time scale than the carrier oscillations. The Fourier series can be truncated at some arbitrarily chosen harmonic of the fundamental carrier frequency, which need not be particularly high in practice. Also, as noted above, the near-resonant behavior of nonlinear systems cannot be meaningfully discussed unless dissipative effects are included. This makes it impossible to use the traveling-wave Ansatz, because the wave must decay as it propagates in the presence of dissipation.

As noted previously, we have avoided some of these difficulties for the moment and have kept the carrier (if it exists) in our pulse throughout the calculations. We introduce the standard staggered-grid finite-difference discretizations of the spatial and temporal time derivatives into the continuum equations (11a) and (11b). This means the electric-field components and the magnetic-field components are spatially separated by $\Delta z/2$ and temporally separated by $\Delta t/2$. We associate the magnetic-field component as being at the "edge" of the cell in the grid; the electric-field component with the "center" of the cell. As a consequence of where the polarization appears in the Maxwell's equations, we associate all of the material properties with the location of the electric field. This means we will treat all of the ρ_i, $i=1,2,3$, as being located with the electric-field values. Many variations of these choices have been tried; the following has been the most accurate and efficient of the approaches we have tested to date. We treat the coupling coefficient γ as being associated with the cell center, the electric-field location. This provides a simple manner in which to specify where the two-level atoms are in the simulation region. Notationally we label, for example, the discrete values of the electric field simply as $E_x(m\Delta z,n\Delta t)\equiv E_x(m,n)$.

Because the exponential decay terms make the Bloch equation numerically stiff, we analytically manipulate the equations before discretizing them by factoring out this exponential behavior. Also, we recognize analytically that the presence of the constant ρ_{30} term in the ρ_3 equation may cause some numerical integration difficulties unless it is multiplied by a term that eventually goes to zero. Introducing the quantities $u_i(z,t)$ through the definitions

$$\rho_1(z,t)=\exp[-t/T_2]u_1(z,t), \tag{A1a}$$

$$\rho_2(z,t)=\exp[-t/T_2]u_2(z,t), \tag{A1b}$$

$$\rho_3(z,t)=\rho_{30}+\exp[-t/T_1]u_3(z,t), \tag{A1c}$$

one obtains the electric-field and two-level atom equations in the form

$$\partial_t E_x=-\frac{1}{\epsilon_0}\partial_z H_y+Au_1-Bu_2, \tag{A2a}$$

$$\partial_t u_1=\omega_0 u_2, \tag{A2b}$$

$$\partial_t u_2=-\omega_0 u_1+C_+E_x u_3+DE_x, \tag{A2c}$$

$$\partial_t u_3=-C_-E_x\rho_2, \tag{A2d}$$

where the time-varying coefficients

$$A(t)=\frac{N_{\text{atom}}\gamma}{\epsilon_0 T_2}\exp\left(-\frac{t}{T_2}\right), \tag{A3a}$$

$$B(t)=\frac{N_{\text{atom}}\gamma\omega_0}{\epsilon_0}\exp\left(-\frac{t}{T_2}\right), \tag{A3b}$$

$$C_+(t)=2\frac{\gamma}{\hbar}\exp\left[-t\left(\frac{1}{T_1}-\frac{1}{T_2}\right)\right], \tag{A3c}$$

$$C_-(t)=2\frac{\gamma}{\hbar}\exp\left[-t\left(\frac{1}{T_2}-\frac{1}{T_1}\right)\right], \tag{A3d}$$

$$D(t)=\frac{\rho_{30}}{T_1}\exp\left(\frac{t}{T_1}\right). \tag{A3e}$$

With the assumed positions for the discrete variables, the magnetic-field equation is solved at the space steps $(m+\frac{1}{2})\Delta z$ for the time steps $(n+\frac{1}{2})\Delta t$. The electric-field and the medium terms ρ_1, ρ_2, and ρ_3 are solved at the space steps $m\Delta z$ for the time steps $n\Delta t$. The discretized version of the Maxwell-Bloch system that we have developed is of the following form.

Maxwell equations.

$$H_y(m+\tfrac{1}{2},n+\tfrac{1}{2})=H_y(m+\tfrac{1}{2},n-\tfrac{1}{2})-\frac{\Delta t}{\mu_0\Delta z}[E_x(m+1,n)-E_x(m,n)], \tag{A4a}$$

$$E_x(m,n+1)=E_x(m,n)-\frac{\Delta t}{\epsilon_0\Delta z}[H_y(m+\tfrac{1}{2},n+\tfrac{1}{2})-H_y(m-\tfrac{1}{2},n+\tfrac{1}{2})]-A(n+\tfrac{1}{2})\tfrac{1}{2}[u_1(m,n+1)+u_1(m,n)]+B(n+\tfrac{1}{2})\tfrac{1}{2}[u_2(m,n+1)+u_2(m,n)]. \tag{A4b}$$

Bloch equations.

$$u_1(m,n+1)=u_1(m,n)+\Delta t\omega_0\tfrac{1}{2}[u_2(m,n+1)+u_2(m,n)], \tag{A4c}$$

$$u_2(m,n+1)=u_2(m,n)-\Delta t\omega_0\tfrac{1}{2}[u_1(m,n+1)+u_1(m,n)]+\Delta tC_+(n+\tfrac{1}{2})\tfrac{1}{2}[E_x(m,n+1)+E_x(m,n)]\times\{\tfrac{1}{2}[u_3(m,n+1)+u_3(m,n)]+D(n+\tfrac{1}{2})\}. \tag{A4d}$$

$$u_3(m,n+1)=u_3(m,n)-\Delta tC_-(n+\tfrac{1}{2})\{\tfrac{1}{2}[E_x(m,n+1)+E_x(m,n)]\times\tfrac{1}{2}[u_2(m,n+1)+u_2(m,n)]\}. \tag{A4e}$$

Notice that there is a mixing of the next and current time-step values in the Maxwell-Bloch equations. This form of the equations does not allow a straightforward leap-frog time integration. It is, however, amenable to a predictor-corrector scheme.

Since the magnetic-field equation is updated at a time different from the other terms in the system (A4), it is advanced in the standard fashion. The remaining system of equations (A4b)–(A4e) is cast into the form

$$U_i^{\text{new}}=U_i^{\text{old}}+\Delta tF_i(\vec{U}^{\text{old}},\vec{U}^{\text{new}}) \quad \text{for} \quad i=1,2,3,4, \tag{A5}$$

where the solution vector components $U_1=E_x$, $U_2=u_1$, $U_3=u_2$, and $U_4=u_3$, and the functionals F_i represent, minus the stand-alone values $\vec{U}^{\text{old}}$, the right-hand sides of (A4b)–(A4e). The coefficients in F are updated and then the values $\vec{U}^{\text{new}}$ are first set equal to their previous time-step values $\vec{U}^{\text{old}}$ in F giving the updated values (A5). These values are compared with the values of $\vec{U}^{\text{new}}$ before the use of (A5), and if the differences are larger than a specified value the process is iterated. We have found that the process converges to give a difference of 0.001% between the previous and new values of $\vec{U}^{\text{new}}$ within 3–4 iterations. The updated values of ρ_1, ρ_2, and ρ_3, are obtained from the inverses of the definitions of u_1, u_2, and u_3 given by Eqs. (A1).

Several other schemes were explored before the present one was obtained. The main selection criteria used to differentiate between the results of these various schemes included satisfaction of the lossless-case constraint $\rho_1^2+\rho_2^2+\rho_3^2=1$ and comparison of the predicted values of ρ_3 after the SIT 2π pulse had passed through the two-level atom medium. The predicted value of $\rho_3=\rho_{30}$ after the passing of the pulse proved to be a sensitive measure of the numerical dispersion. Errors in the residual levels of the electric-field and polarization terms prevent a complete return to the ground state from the inverted state in the 2π-pulse case. The predictor-corrector scheme not only produced the smallest errors in these terms, but also required the least amount of discretization. The choice of $\lambda/200$ for the discretization was made to give very accurate results. Acceptable results have been obtained with a specification of $\Delta z=\lambda/50$ for many of the cases we investigated.

[1] R. W. Ziolkowski and J. B. Judkins, J. Opt. Soc. Am. B **10**, 186 (1993).

[2] R. W. Ziolkowski and J. B. Judkins, *Integrated Photonics Research Post-Deadline Papers, 1992* (Optical Society of America, Washington, D.C., 1992), pp. 50–51.

[3] R. W. Ziolkowski and J. B. Judkins, *Integrated Photonics Research Technical Digest, 1993* (Optical Society of America, Washington, D.C., 1993), pp. 128–131.

[4] R. W. Ziolkowski and J. B. Judkins, Radio Sci. **28**, 901 (1993).

[5] R. W. Ziolkowski and J. B. Judkins, J. Opt. Soc. Am. B **11**, 1565 (1994).

[6] P. M. Goorjian and A. Taflove, Opt. Lett. **17**, 180 (1992).

[7] P. M. Goorjian, A. Taflove, R. M. Joseph, and S. C. Hagness, IEEE J. Quantum Electron **QE-28**, 2416 (1992).

[8] R. M. Joseph, P. M. Goorjian, and A. Taflove, Opt. Lett. **18**, 491 (1993).

[9] C. V. Hile and W. L. Kath, *Integrated Photonics Research Technical Digest, 1993* [3], pp. 308–311.

[10] S. Radic and N. George, Opt. Lett. **19**, 1064 (1994).

[11] S. A. Basinger and D. J. Brady, J. Opt. Soc. Ann. A **11**, 1504 (1994).

[12] R. P. Feynman, F. L. Vernon, Jr., and R. W. Hellwarth, J. Appl. Phys. **28**, 49 (1957).

[13] G. L. Lamb, Phys. Lett. **25A**, 181 (1967).

[14] D. Burnham and R. Chiao, Phys. Rev. **188**, 667 (1969).
[15] J. A. Fleck, Jr., Phys. Rev. B **1**, 84 (1970).
[16] G. L. Lamb, Rev. Mod. Phys. **43**, 99 (1971).
[17] J. C. Eilbeck and R. K. Bullough, J. Phys. A **5**, 820 (1972).
[18] R. A. Smith, Proc. R. Soc. London Ser. A **362**, 1 (1978).
[19] H. A. Haus, Rev. Mod. Phys. **51**, 331 (1979).
[20] A. Yariv, *Quantum Electronics*, 2nd ed. (Wiley, New York 1967), pp. 149–156, 371–382, 388–405.
[21] P. N. Butcher and D. Cotter, *The Elements of Nonlinear Optics* (Cambridge University Press, Cambridge, England, 1991), pp. 156–172.
[22] P. W. Milonni and L. E. Thode, Appl. Opt. **31**, 785 (1992).
[23] L. C. Bradley, J. Opt. Soc. Am. B **9**, 1931 (1992).
[24] R. J. Temkin, J. Opt. Soc. Am. B **10**, 830 (1993).
[25] P. W. Milonni and J. H. Eberly, *Lasers* (Wiley, New York, 1988), pp. 243–260.
[26] A. D. Buckingham, Adv. Chem. Phys. **12**, 107 (1967).
[27] A. D. Buckingham and M. B. Dunn, J. Chem. Soc. A 1988 (1971).
[28] E. B. Graham and R. E. Raab, J. Appl. Phys. **69**, 2549 (1991).
[29] E. B. Graham and R. E. Raab, Philos. Mag. B **64**, 267 (1991).
[30] R. J. Hawkins and J. S. Kallman, Opt. Quantum Electron. **26**, S207 (1994).
[31] A. E Siegman, *Lasers* (University Science Books, Mill Valley, CA, 1986), p. 292.
[32] F. T. Hioe and J. H. Eberly, Phys. Rev. A **25**, 2168 (1982).
[33] P. K. Aravind, J. Opt. Soc. Am. B **3**, 1025 (1986).